The Effects of Rainfall Inhomogeneity on Climate Variability of Rainfall Estimated from Passive Microwave Sensors

CHRISTIAN KUMMEROW

Department of Atmospheric Science, Colorado State University, Fort Collins, Colorado

PHILIP POYNER

USAF, Vandenberg AFB, California

WESLEY BERG AND JODY THOMAS-STAHLE

Department of Atmospheric Science, Colorado State University, Fort Collins, Colorado

(Manuscript received 30 July 2003, in final form 7 November 2003)

ABSTRACT

Passive microwave rainfall estimates that exploit the emission signal of raindrops in the atmosphere are sensitive to the inhomogeneity of rainfall within the satellite field of view (FOV). In particular, the concave nature of the brightness temperature (T_b) versus rainfall relations at frequencies capable of detecting the blackbody emission of raindrops cause retrieval algorithms to systematically underestimate precipitation unless the rainfall is homogeneous within a radiometer FOV, or the inhomogeneity is accounted for explicitly. This problem has a long history in the passive microwave community and has been termed the beam-filling error. While not a true error, correcting for it requires a priori knowledge about the actual distribution of the rainfall within the satellite FOV, or at least a statistical representation of this inhomogeneity. This study first examines the magnitude of this beam-filling correction when slant-path radiative transfer calculations are used to account for the oblique incidence of current radiometers. Because of the horizontal averaging that occurs away from the nadir direction, the beam-filling error is found to be only a fraction of what has been reported previously in the literature based upon plane-parallel calculations. For a FOV representative of the 19-GHz radiometer channel (18 km $\times$ 28 km) aboard the Tropical Rainfall Measuring Mission (TRMM), the mean beam-filling correction computed in this study for tropical atmospheres is 1.26 instead of 1.52 computed from plane-parallel techniques. The slant-path solution is also less sensitive to finescale rainfall inhomogeneity and is, thus, able to make use of 4-km radar data from the TRMM Precipitation Radar (PR) in order to map regional and seasonal distributions of observed rainfall inhomogeneity in the Tropics. The data are examined to assess the expected errors introduced into climate rainfall records by unresolved changes in rainfall inhomogeneity. Results show that global mean monthly errors introduced by not explicitly accounting for rainfall inhomogeneity do not exceed 0.5% if the beam-filling error is allowed to be a function of rainfall rate and freezing level and does not exceed 2% if a universal beam-filling correction is applied that depends only upon the freezing level. Monthly regional errors can be significantly larger. Over the Indian Ocean, errors as large as 8% were found if the beam-filling correction is allowed to vary with rainfall rate and freezing level while errors of 15% were found if a universal correction is used.

1. Introduction

Climate studies of rainfall trends and variability require satellite-based products in order to overcome the extremely limited in situ observations over the world's oceans. Because passive microwave observations are directly correlated to the amount of liquid water in the rain column, methods such as those developed by Wilheit et al. (1991), Kummerow et al. (2001), or Petty (1994) have been favored over infrared techniques that have good temporal sampling but poor physical relations with the actual rain. To make optimal use of both types of sensors, the Global Precipitation Climatology Project (GPCP) (Huffman et al. 1997) merges the passive microwave results with infrared data but only after using the microwave results to remove any regional biases from the infrared data. The utility of passive microwave sensors can also be inferred from the ever-increasing number of sensors. As of this writing, there are three Special Sensor Microwave Imager (SSM/I) instruments in orbit in addition to the Tropical Rainfall Measuring Mission (TRMM) Microwave Imager (TMI), the Japanese Advanced Microwave Sounding Radiometer

Corresponding author address: Christian Kummerow, Dept. of Atmospheric Science, Colorado State University, Fort Collins, CO 80523-1371.
E-mail: kummerow@atmos.colostate.edu

(AMSR-E) aboard the *Aqua* satellite, and a similar instrument aboard the Japanese *Advanced Earth Observing Satellite-II* (*ADEOS-II*). Despite their increasing use, however, passive microwave estimates are not free of uncertainties as they contain a number of implicit assumptions related to cloud morphology and microphysical properties. To the extent that real cloud systems deviate from these assumptions, one must expect errors in the microwave products. These errors vary from random, which reflect deviations of individual clouds from the norm, to ocean-basin- and global-scale variations associated with large-scale changes in precipitation cloud properties. It is hypothesized that these large-scale changes in cloud properties are in response to large-scale changes in the external forcing mechanisms as might be evidenced during an El Niño–Southern Oscillation (ENSO) event.

Recent data from the TRMM satellite (Kummerow et al. 2000) make it possible to examine large-scale differences in rainfall derived from two very distinct sensors—the TMI and the TRMM Precipitation Radar (PR). While neither is considered ''truth'' in this study, their differences can be studied at the large space and time scales important for climate applications. Because the TMI and PR sense very different aspects of precipitating clouds, any systematic differences between these two sensors are likely caused by changes in the underlying cloud morphology or microphysics that cannot be directly observed by one or both sensors. Figure 1a shows the temporal deviations of the mean tropical rainfall derived from the two passive microwave and radar algorithms used by the TRMM project. The two passive microwave algorithms are those of Wilheit et al. (1991) designed for monthly $5° \times 5°$ accumulations and Kummerow et al. (2001), which is optimized for instantaneous retrievals. The algorithms use the same input data but are quite distinct in their philosophy. The Wilheit et al. (1991) scheme, known as the TRMM 3A11 product, exploits the observed warming of brightness temperature T_b at 19 GHz due to the blackbody emission of raindrops over a radiometrically cold ocean. The scheme uses a simple conceptual cloud model to construct the T_b versus rainfall relations. While prone to large errors at the pixel level, its strength is in its simplicity and the large reduction of random errors that occurs for satellite rainfall estimates over large space and time domains. In contrast, the Kummerow et al. (2001) approach, known as the TRMM 2A12 product, tries to optimize the pixel-level retrievals by fully accounting for all channels on the TRMM radiometer. This is accomplished by a Bayesian inversion methodology that introduces a priori information from a set of precomputed cloud-resolving model profiles. The added complexity is beneficial for pixel-level retrievals, but the long-term stability of it in the algorithm is more difficult to verify. As such, the two approaches are highly complementary. The TRMM PR product, known as 2A25, uses a Z–R-type approach but modifies the originally assumed relation when the total path attenuation is sufficiently robust to constrain the solution. As such, the algorithm is susceptible to changes in the rainfall drop size distribution, particularly for light to moderate rainfall rates where the total path attenuation cannot be distinguished from the background noise. Robertson et al. (2003) have examined this issue and found some evidence that changes in the drop size distribution might indeed be occurring that are not being captured by the PR algorithm.

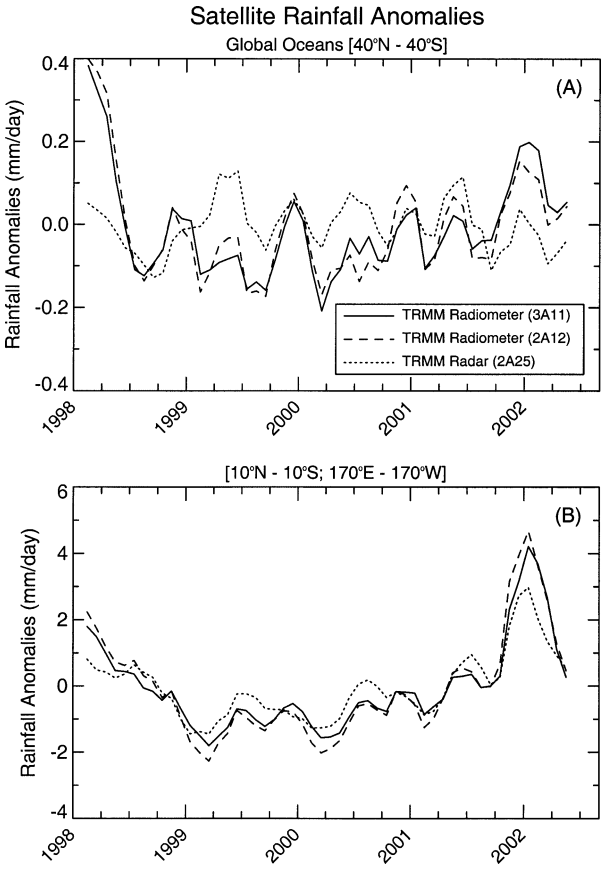

FIG. 1. Time series for two TRMM radiometers and the TRMM radar rainfall products for (a) the global oceans between 36°N and 36°S, and (b) a $20° \times 20°$ area in the central Pacific.

Figure 1a shows deviations for each of the three algorithms discussed above from their own 4-yr climatologies. These variability plots clearly show that the two passive microwave algorithms agree quite well in their global trends, but the PR shows a significantly reduced variability. The greatest differences appear at the height of the El Niño event of 1997–98 at the beginning of the time series. At these large scales, sampling differences between TMI and PR are negligible, and the details of the inversion approach do not appear to be as important as the basic data used. As such, this behavior is consistent with the hypothesis that these differences are not caused by specific algorithm errors but rather by the large-scale systematic changes in rain-

fall morphology or microphysics that are assumed constant by one or both of the sensors. A difference of approximately 0.3 mm day^{-1}, or 10% of the mean global rainfall, however, has important consequences. Soden (2000) found that this was the magnitude of disagreement between climate models and observations associated with the 1982–83 ENSO event. Yet, despite the large differences in rainfall variability at the tropical ocean scale shown in Fig. 1a, these differences are not uniform in space. If one focuses on a 20° × 20° region in the central Pacific between 170°E and 170°W and ±10° latitude, one finds substantially improved trend correlations between the sensors as is shown in Fig. 1b. Within the current hypothesis, such behavior would be expected if only the total rainfall changed while the cloud morphology and microphysics remain relatively constant during this period.

In order to resolve what appear to be regional biases and trends related to changes in cloud properties, assumed to be constant, a systematic analysis of potential errors must be undertaken. Ground-based observations over oceans, because of their limited spatial and temporal coverage, can hardly be expected to resolve differences that are regionally and temporally varying with correlation lengths far larger than a ground-based system can observe. Instead, an error-characterization strategy is needed to build an independent error model for rainfall estimates that considers the earth system in its entirety. In this paradigm, instead of relying on ground-based comparisons, the assumptions in the algorithms are examined one at a time until a comprehensive error model can be put forth based on first principles. The role of ground validation in this paradigm shifts from one of providing point comparisons with satellite products to one in which they are used to verify the hypotheses and procedures used in the global error characterization.

Some assumptions in the algorithms can be shown to have relatively little impact upon the computed radiances. In this case, one can allow a generous uncertainty in the assumed parameter without introducing much uncertainty in the retrieval. In other cases, the assumed variables affect retrievals in a substantial manner and error propagation models lead to excessive uncertainties unless the assumed parameter is somehow constrained to reflect its actual variability instead of its potential variability. Rainfall inhomogeneity is such a parameter. The assumed rainfall inhomogeneity within relatively large (10–60 km) footprints of current microwave radiometers can lead to significant errors in the retrieved rainfall products. These errors are related to the nonlinear relation between the brightness temperatures, T_b, and rainfall. The bias, resulting from nonuniform beam filling, was first described by Wilheit (1986). While Spencer et al. (1983) had also observed this bias, that study focused only on the partial beam filling by uniform rainshowers within the radiometer field of view (FOV) and did not offer a coherent explanation of the effect. Since then, numerous authors including Chiu et al. (1990), Graves (1993), Petty (1994), Ha and North (1995), North and Polyak (1996), and Kummerow (1998) have all looked at this problem from theoretical as well as statistical considerations. As such, the problem is thought to be theoretically well understood, and in principle, the error propagation model is simple. Unfortunately, the rainfall variability is not a simple function of rainfall rate and can be shown (section 3) to vary both regionally and temporally. As such, it is not simply enough to understand the theoretical basis for the beam-filling error, but quantitative global statistics of rainfall inhomogeneity at scales below current FOV sizes are needed in order to assess the actual impact of this uncertainty upon rainfall products at various space and time scales. The magnitude of the error introduced by this uncertain subresolution variability will eventually depend both upon the theoretical foundation of this error, as well as the extent to which the climate system allows changes in rainfall variability to occur at various time and space scales.

This study makes use of the relatively high resolution TRMM PR data to serve as a proxy for the actual rainfall variability within the TRMM TMI footprint, which is 18 km × 30 km for the 19-GHz channels (approximated by a square area of 24 km × 24 km for computational simplicity in this study). Before undertaking an examination of the observed variability and its consequences for regional and global biases, however, section 2 of this paper provides a brief review of the theoretical basis of the beam-filling correction, including the effects of using one-dimensional radiative transfer models to treat a problem that is inherently three-dimensional. Section 3 examines PR-observed rainfall inhomogeneity to look for both regional and interannual variation. A discussion and conclusions are presented in section 4.

2. The beam-filling error

A passive microwave sensor's ability to measure rainfall over oceans depends on the blackbody emission of liquid drops, which offer a strong contrast to radiometrically cold ocean surfaces at these wavelengths. Irrespective of the inversion details, all physically based retrieval algorithms begin with radiative transfer computations to establish relationships between an assumed cloud structure and the satellite-observed T_b. Wilheit (1986) described the simple conceptual rainfall cloud used in this study. In that cloud, a Marshall–Palmer (Marshall and Palmer 1948) distribution of raindrops is assumed from the surface up to the freezing level (0°C isotherm). Density of water is adjusted to keep a constant rainfall rate throughout the column. A standard lapse rate of 6.5 K km^{-1} was specified and the relative humidity was assumed to be 80% at the surface, increased linearly to 100% at the freezing level, and remained at 100% above that. A nonprecipitating cloud layer containing 0.5 g m^{-3} of cloud liquid water is as-

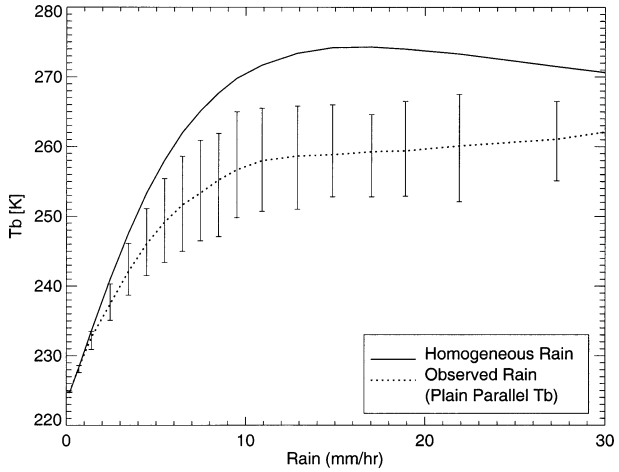

FIG. 2. Upwelling T_b computed from plane-parallel theory for a 24 km $\times$ 24 km FOV assuming a uniform rain field (solid curve) as well as the actual observed sub-FOV inhomogeneity (dotted line).

sumed in the 0.5 km just below the freezing level, while variable amounts of ice can be specified above the freezing level. Because it is not specified in the Wilheit (1986) paper, we assume that the ice extends 3 km above the freezing level with amounts equal to 0.75, 0.5, and 0.25 times the rainwater content in each successive kilometer above the freezing level. Ice is modeled as graupel with a density of 0.4 g cm^{-3} with a Marshall–Palmer drop size distribution. These assumptions thus couple the surface temperature, the freezing level, and the precipitable and cloud water contents of the atmosphere. The rainfall intensity couples the total rainwater content to the ice aloft. Specifying a surface temperature and a rainfall rate determines all cloud parameters in the model.

a. Plane-parallel approximation

A plane-parallel Eddington approximation (Kummerow 1993) is used for the radiative transfer computations. The radiative approximation introduces errors of less than 1–2 K for the frequencies examined in this study (Smith et al. 2002). The effect of using a plane-parallel computation to examine inhomogeneous rainfall, which is inherently three-dimensional, is examined separately. The atmospheric model described above specifies all the input parameters to the radiative transfer equations except for the surface emissivity which, in turn, depends upon the near-surface wind speed. Here, we use a wind speed of 6 m s^{-1} to represent average oceanic conditions. Oxygen and water vapor absorption are computed from Liebe et al. (1993) while cloud water absorption is specified by Rayleigh theory. The absorption in this regime is independent of particle sizes. Scattering parameters for raindrop and graupel particles are computed from Mie (1908) theory.

Figure 2 shows the relations between theoretically derived T_b and area mean rainfall assuming either homogeneous rain (solid curve) or inhomogeneous rain (dashed curve) where the actual rainfall distribution is taken from 4-km PR data. The solid curve in Fig. 2 shows the computed T_b corresponding to the cloud model described above for 19.35-GHz, vertically polarized radiation with a view angle of 53° over an ocean background. The computations were made assuming a sea surface temperature of 302 K (freezing level of 4.5 km) thought to be representative of the Tropics. The dashed line in the figure corresponds to the average T_b in a 24 km $\times$ 24 km FOV computed from 4-km TRMM PR rainfall data. The appropriate model corresponding to the PR surface rainfall is used for each PR pixel and plane-parallel radiative transfer computations are performed for each 4 km $\times$ 4 km pixel before the T_b are averaged to the radiometer FOV. The rainfall plotted on the horizontal axis in this case is the FOV-averaged rainfall. The fact that the T_b curve corresponding to nonuniform rainfall is always below the uniform rainfall curve is predicated by the concave nature of the uniform rainfall relation. Inversion schemes that attempt to invert the radiance signal based upon uniform rainfall assumptions will therefore infer lower rainfall rates than the true rainfall as indicated by the dashed line. Unlike the uniform rainfall curve, which is fully determined by the conceptual cloud, the nonuniform rainfall curve shows considerable variability that results from different realizations within a given FOV leading to the same mean rainfall. The fact that the tops of the error bars are typically well below the homogeneous rainfall curve for all but the lightest rain cases (low T_b) implies that homogeneous rainfall rarely occurs at a scale of 24 km $\times$ 24 km. Mean T_b and variances were computed for 3 months of oceanic PR data from December 1999 through February 2000. Only the six pixels on each side of nadir were used for this purpose. All freezing levels were assumed to be 4.5 km for these calculations.

Because of the bias introduced when homogeneous rainfall is assumed in the radiative transfer computations for rain fields that are not homogeneous, a beam-filling correction can be defined to account for this bias if the variability is known. The beam-filling correction was obtained in this study by computing the T_b from the inhomogeneous FOV and inverting it to obtain a rainfall rate following the homogeneous rainfall curve (i.e., solid line). The ratio of the true rainfall rate to that inferred from the homogeneous rainfall curve constitutes the beam-filling correction. Following Chiu et al. (1990) the data were binned by mean rainfall, $\langle R \rangle$, and rainfall inhomogeneity parameter, Ψ, defined for a given satellite FOV by $\Psi = \sigma_R / \langle R \rangle$, where σ_R is the standard deviation of the individual high-resolution measurements:

$$\sigma_R = \left[\frac{1}{N-1} \sum_{n=1}^{36} (R_n - \langle R \rangle)^2 \right]^{0.5}.$$

Here, $N = 36$ because 4-km rain data within a 24 km $\times$ 24 km satellite FOV are used. Table 1 presents the actual values for the beam-filling correction as a function of mean rainfall rate, $\langle R \rangle$, and inhomogeneity parameter, Ψ. Within each $\langle R \rangle$ and Ψ category, the standard deviation of the mean beam-filling correction is quite small relative to changes in the rainfall categories. This is consistent with the results of Chiu et al. (1990), who showed from theoretical considerations that the above two parameters should fully specify the beam-filling correction if the rainfall follows a well-defined statistical distribution with the satellite FOV.

The beam-filling corrections shown in Table 1 are a strong function of the mean rainfall rate as well as the inhomogeneity parameter. Unfortunately, the inhomogeneity parameter cannot be determined by the radiometer itself. In order to develop a mean correction for this effect, Chiu et al. (1990) used mean statistics from 4-km shipborne radar data obtained during the Global Atmospheric Research Program (GARP) Atlantic Tropical Experiment (GATE) to compute corrections applicable to various FOV sizes. For a 24 km $\times$ 24 km FOV, their results indicate a mean correction of approximately 1.54 or 1.68 depending upon which intensive observing period (IOP) was selected. This compares well to a mean value of 1.52 computed from the PR data described above if all raining pixels are used. A value of 1.60 is obtained if only pixels with rainfall in excess of 0.5 mm h^{-1} are used in the calculations. The 0.5 mm h^{-1} criterion corresponds roughly to the limit of detectability of passive microwave radiometers. The mean corrections in both cases are computed by weighting the values, as computed in Table 1, with the appropriate distribution of observed $\langle R \rangle$ and Ψ in the 24 km $\times$ 24 km FOV. These corrections, however, assume a plane-parallel radiative transfer solution. If interactions between neighboring clouds are allowed, the correction factors will be seen in the next section to decrease rather substantially from the above values.

b. Slant-path approximation

The nature of the Eddington approximation is such that diffuse radiances are computed first. Once the diffuse radiance is known, the upwelling T_b are computed by tracing individual rays through the cloud allowing for emission, absorption, scattering out of the beam, and scattering back into the direction of view from previously computed diffuse radiation. As such, the Eddington approximation is amenable to a pseudo-three-dimensional version in which the diffuse radiance is computed as if each pixel were independent and horizontally infinite, but the ray tracing is done through the actual three-dimensional structure of the cloud. This approximation was used by Bauer et al. (1998) who found excellent agreement with a full three-dimensional backward Monte Carlo code developed previously by Roberti et al. (1994). The pseudo-three-dimensional Eddington approximation, referred to as the slant-path approximation, is used here because of the prohibitive cost of running the Monte Carlo code for 3 months of PR data representing approximately 40 000 individual radiometer FOVs. For typical view angles around 53° used by spaceborne radiometers, the slant path through the raining clouds is expected to average radiation from neighboring pixels and thus smooth out the upwelling radiance field—particularly if horizontal dimensions are significantly smaller than the height of the rain column.

Following the procedure of the previous section, Fig. 3 shows the T_b computed from the slant-path approximation and compares it to the homogeneous rainfall case. Because periodic boundary conditions are assumed by the slant-path code, the homogeneous rainfall curve matches the plane-parallel result. The T_b computed from the slant-path approximation, however, are significantly closer to the homogeneous curve due to the horizontal averaging that takes place as radiation crosses the cloud along a slanted path. Alternatively, the slanted-path averaging has the same effect as reducing the inhomogeneity parameter Ψ. This can also be confirmed in Table 2, which presents the quantitative beam-filling corrections as a function of $\langle R \rangle$ and Ψ. The corrections are smaller for each $\langle R \rangle$ and Ψ, as well as for the mean global beam-filling correction. For the slant-path approximation, the mean beam-filling correction is 1.26 when all raining pixels are considered, and 1.29 if a rain threshold of 0.5 mm h^{-1} is assumed. Qualitatively, this result is in agreement with a previous study by Petty (1994), who used three-dimensional computations to conclude that radiation escaping from the sides of clouds would lead to beam-filling corrections much smaller than what is inferred from plane-parallel calculations. Quantitatively, these values are consistent with the TRMM operational algorithm developed by Wilheit et al. (1991). The beam-filling correction of this algorithm is based on slant-path calculations performed by Wang (1996) using aircraft radar data obtained during the Tropical Ocean Global Atmosphere Coupled Ocean–Atmosphere Response Experiment (TOGA COARE). For TMI, the correction factor is given by $1 + 0.062 \times$ freezing height (Chang and Chiu 2001), which results in a value of 1.28 for a freezing height of 4.5 km used in this study. Results are also consistent with aircraft radar data from the Kwajalein Experiment (KWAJEX) evaluated by Chen (2001) who found only a 4% difference between TOGA COARE and KWAJEX observations.

Because of differences between the plane-parallel and slant-path approaches, there is the potential to significantly alter some of the current satellite rainfall products. There is, however, no clear path between the numbers presented here and the impact upon a specific algorithm. This is because most algorithms convolve the beam-filling correction with other corrections and uncertainties. As such, the numbers presented here must be analyzed in terms of each specific algorithm to assess

TABLE 1. Mean beam-filling correction factor and standard deviation computed as a function of the average rainfall, $\langle R \rangle$, and the inhomogeneity parameter, Ψ, using plane-parallel radiative transfer calculations. Entries in parentheses indicate fewer than 10 data points. An absent standard deviation (± —) indicates that only one data point was available while blank entries indicate that no data were available for that category.

Rain rate (mm h^{-1})	Inhomogeneity parameter									
	0.0–0.5	0.5–1.0	1.0–1.5	1.5–2.0	2.0–2.5	2.5–3.0	3.0–3.5	3.5–4.0	4.0–5.0	5.0–6.0
0–0.5	(1.00 ± —)	1.00 ± 0.00	1.00 ± 0.00	1.00 ± 0.00	1.00 ± 0.01	1.00 ± 0.01	1.01 ± 0.02	1.01 ± 0.04	1.02 ± 0.06	1.05 ± 0.12
0.5–1	1.00 ± 0.00	1.00 ± 0.00	1 ± 0.01	1.02 ± 0.03	1.07 ± 0.05	1.14 ± 0.08	1.24 ± 0.11	1.38 ± 0.15	1.64 ± 0.24	2.20 ± 0.25
1–2	1.00 ± 0.01	1.02 ± 0.02	1.07 ± 0.05	1.17 ± 0.08	1.30 ± 0.12	1.49 ± 0.17	1.72 ± 0.22	2.07 ± 0.31	(2.57 ± 0.42)	(3.28 ± 0.12)
2–3	1.02 ± 0.01	1.07 ± 0.03	1.21 ± 0.07	1.42 ± 0.11	1.71 ± 0.18	2.03 ± 0.21	2.34 ± 0.26	2.93 ± 0.54	(3.69 ± 0.64)	
3–4	1.04 ± 0.01	1.13 ± 0.05	1.35 ± 0.10	1.64 ± 0.15	2.04 ± 0.24	2.34 ± 0.28	2.74 ± 0.51	(3.36 ± 0.71)	(4.62 ± —)	
4–5	1.06 ± 0.02	1.19 ± 0.07	1.51 ± 0.13	1.92 ± 0.28	2.36 ± 0.35	2.56 ± 0.30	(3.09 ± 0.68)	(2.75 ± 0.02)	(5.54 ± —)	
5–6	1.08 ± 0.02	1.25 ± 0.09	1.63 ± 0.17	2.06 ± 0.27	2.71 ± 0.49	(3.56 ± 0.87)	(3.85 ± 0.50)		4.81 ± 1.13	
6–7	1.09 ± 0.03	1.30 ± 0.11	1.76 ± 0.22	2.27 ± 0.33	2.99 ± 0.63	(3.95 ± 1.08)	(4.43 ± 0.08)			
7–8	1.11 ± 0.04	1.37 ± 0.13	1.89 ± 0.26	2.44 ± 0.37	2.96 ± 0.51	(4.97 ± 1.99)	(4.78 ± 0.16)	(2.91 ± —)		
8–9	1.13 ± 0.05	1.43 ± 0.16	1.93 ± 0.29	2.54 ± 0.45	3.52 ± 0.94	(3.11 ± 0.09)	(5.27 ± —)			
9–10	1.16 ± 0.05	1.46 ± 0.14	2.11 ± 0.31	2.79 ± 0.46	(3.06 ± 0.36)					
10–12	1.20 ± 0.08	1.57 ± 0.20	2.28 ± 0.38	3.02 ± 0.55	3.75 ± 1.12	(3.26 ± —)				
12–14	1.26 ± 0.08	1.72 ± 0.26	2.58 ± 0.37	3.54 ± 0.82	(3.58 ± 0.87)					
14–16	(1.42 ± 0.04)	2.00 ± 0.31	2.80 ± 0.50	3.45 ± 0.82						
16–18	(1.54 ± —)	2.36 ± 0.40	2.94 ± 0.44	4.04 ± 0.82	(4.97 ± 0.58)					
18–20	(1.66 ± —)	(2.61 ± 0.38)	3.30 ± 0.60	(3.37 ± 0.13)	(7.64 ± 2.21)	(4.97 ± —)				
20–25	(1.90 ± 0.16)	(2.58 ± 0.39)	3.73 ± 0.80	(5.30 ± 1.37)	(7.20 ± 1.64)					
25–30		3.63 ± 0.76	5.26 ± 0.90							
30–35		(4.16 ± 0.34)	(5.01 ± —)	(7.34 ± —)						
35–40		(4.72 ± 0.13)	(5.47 ± 0.32)							
40–45		(5.93 ± 0.21)	(6.54 ± —)							
45–50			(8.25 ± 1.00)							

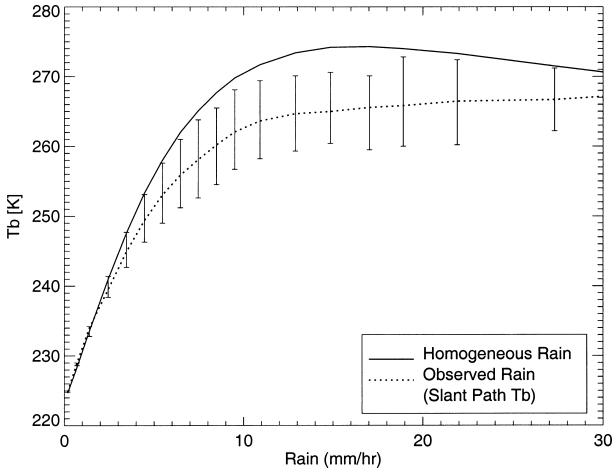

FIG. 3. Upwelling T_b computed from slant-path radiative transfer methods for a 24 km × 24 km FOV assuming a uniform rain field (solid curve) as well as the actual observed sub-FOV inhomogeneity (dotted line).

the degree to which the algorithm would change with the new beam-filling correction employed and the extent to which other global assumptions can offset any changes in the mean beam-filling correction. The often arbitrary shape of the vertical distribution of rainwater with height, for instance, could easily lead to higher or lower surface rainfall rates for the same retrieved liquid water content.

c. Sensitivity to data resolution

TRMM radar data at 4 km are available over the entire Tropics. As such, they are ideally suited to study the global behavior of the beam-filling correction. The data cannot, however, address the question of whether the data itself have sufficient spatial resolution to properly quantify the beam-filling correction. To address this, 250-m-resolution ground-based radar data were collected as part of the AMSR-E rainfall validation effort in March–April 2001 at Wallops Island, Virginia (Matrosov et al. 2002). While this dataset is limited in its spatial and temporal domain, it can be used to study the behavior of the beam-filling correction when higher-resolution data are available. The rainfall products were produced from the dual-polarization X-band radar belonging to the National Oceanic and Atmospheric Administration's Environmental Technology Laboratory (NOAA/ETL) using standard polarimetric techniques out to a range of 40 km from the radar (Matrosov et al. 2002).

Based on the physical principles discussed by Chiu et al. (1990) and the results from previous sections, one would expect the mean rainfall, $\langle R \rangle$, and variability parameter, Ψ, to fully determine the beam-filling correction regardless of the initial resolution of the data. This is confirmed in Table 3, which shows a subset of the mean beam-filling correction computed from the Wallops radar data for rainfall rates in the range of 3–4 mm h^{-1} and inhomogeneity parameters in the range of 0–3.0. The table was generated for various initial radar data resolutions in which values lower than 250 m were obtained by simply averaging the initial 250-m data. For comparison purposes, the freezing level was assumed to be the same 4.5 km value assumed earlier. Values are within the standard deviation of those found using PR data in the previous sections. However, the inhomogeneity parameter itself is somewhat different depending upon the original resolution of the data. This can be seen in Table 3 by examining the number of occurrences (in parentheses) corresponding to each rainfall inhomogeneity category. As the original resolution decreases, more and more pixels fall into lower inhomogeneity categories as would be expected since the inhomogeneity must be zero in the limit that 24-km data are used as the initial measurement.

Table 4 shows the total impact of changing the original resolution upon the beam-filling correction when averaged over the observed inhomogeneity parameter. Because the beam-filling correction does not change significantly as a function of $\langle R \rangle$ and Ψ, the table primarily reflects changes in the computed inhomogeneity parameter. In the plane-parallel case, the gradual increase in the computed inhomogeneity with resolution is seen to have a substantial effect upon the mean beam-filling correction for the rainfall rates (2–6 mm h^{-1}) presented. The beam-filling correction captured by 4-km data can be seen to be only 57% of the true beam-filling correction for the rainfall category 2–3 mm h^{-1}, 60% for 3–4 and 4–5 mm h^{-1}, and 70% for the 5–6 mm h^{-1} category. In contrast to the plane-parallel calculations, this effect has all but disappeared for the slant-path calculations and the beam-filling correction computed from 4-km data is seen to faithfully reproduce the 250-m inferred corrections. Only minimal changes can be observed in going from 250-m data to 4-km data in the slant-path calculations. The fact that it appears to be completely insensitive to the original resolution may be due to the lack of robust statistics from a single field experiment once rainfall is stratified by mean rainfall and inhomogeneity parameter. Even with more robust statistics, however, the change in the computed beam-filling correction with increased resolution should be significantly smaller than it is for the plane-parallel approximation.

d. Sensitivity to freezing level

The beam-filling correction, because it has its origin in the blackbody emission of liquid water drops, is not sensitive to the surface rainfall, but to the integrated liquid water. As such, one can speak of the sensitivity to rainfall only because the conceptual cloud model defined by Wilheit (1986) couples the surface rainfall to the integrated water content. For lower freezing levels, however, the previously computed results, assuming a

TABLE 2. Mean beam-filling correction factor and standard deviation computed as a function of the average rainfall, $\langle R \rangle$, and the inhomogeneity parameter, Ψ, using slant-path radiative transfer calculations. Entries in parentheses indicate fewer than 10 data points. An absent standard deviation (± —) indicates that only one data point was available while blank entries indicate that no data were available for that category.

Rain rate (mm h^{-1})	Inhomogeneity parameter									
	0.0–0.5	0.5–1.0	1.0–1.5	1.5–2.0	2.0–2.5	2.5–3.0	3.0–3.5	3.5–4.0	4.0–5.0	5.0–6.0
0–0.5	(1.00 ± —)	1.00 ± 0.00	1.00 ± 0.00	1.00 ± 0.00	1.00 ± 0.00	1.00 ± 0.01	1.01 ± 0.02	1.01 ± 0.04	1.02 ± 0.06	1.05 ± 0.12
0.5–1	1.00 ± 0.00	1.00 ± 0.00	1 ± 0.01	1.02 ± 0.03	1.07 ± 0.05	1.14 ± 0.08	1.24 ± 0.11	1.38 ± 0.15	1.64 ± 0.24	2.20 ± 0.25
1–2	1.00 ± 0.01	1.02 ± 0.02	1.07 ± 0.05	1.17 ± 0.08	1.30 ± 0.12	1.49 ± 0.17	1.72 ± 0.22	2.07 ± 0.31	2.57 ± 0.42	(3.28 ± 0.12)
2–3	1.02 ± 0.01	1.07 ± 0.03	1.21 ± 0.07	1.42 ± 0.11	1.71 ± 0.18	2.03 ± 0.21	2.34 ± 0.26	2.93 ± 0.54	(3.69 ± 0.64)	
3–4	1.04 ± 0.01	1.13 ± 0.05	1.35 ± 0.10	1.64 ± 0.15	2.04 ± 0.24	2.34 ± 0.28	2.74 ± 0.51	(3.36 ± 0.71)	(4.62 ± —)	
4–5	1.06 ± 0.02	1.19 ± 0.07	1.51 ± 0.13	1.92 ± 0.28	2.36 ± 0.35	2.56 ± 0.30	(3.09 ± 0.68)	(2.75 ± 0.02)	(5.54 ± —)	
5–6	1.08 ± 0.02	1.25 ± 0.09	1.63 ± 0.17	2.06 ± 0.27	2.71 ± 0.49	(3.56 ± 0.87)	(3.85 ± 0.50)		4.81 ± 1.13	
6–7	1.09 ± 0.03	1.30 ± 0.11	1.76 ± 0.22	2.27 ± 0.33	2.99 ± 0.63	(3.95 ± 1.08)	(4.43 ± 0.08)			
7–8	1.11 ± 0.04	1.37 ± 0.13	1.89 ± 0.26	2.44 ± 0.37	2.96 ± 0.51	(4.97 ± 1.99)	(4.78 ± 0.16)	(2.91 ± —)		
8–9	1.13 ± 0.05	1.43 ± 0.16	1.93 ± 0.29	2.54 ± 0.45	3.52 ± 0.94	(3.11 ± 0.09)	(5.27 ± —)			
9–10	1.16 ± 0.05	1.46 ± 0.14	2.11 ± 0.31	2.79 ± 0.46	(3.06 ± 0.36)					
10–12	1.20 ± 0.08	1.57 ± 0.20	2.28 ± 0.38	3.02 ± 0.55	3.75 ± 1.12	(3.26 ± —)				
12–14	1.26 ± 0.08	1.72 ± 0.26	2.58 ± 0.37	3.54 ± 0.82	(3.58 ± 0.87)					
14–16	(1.42 ± 0.04)	2.00 ± 0.31	2.80 ± 0.50	3.45 ± 0.82						
16–18	(1.54 ± —)	2.36 ± 0.40	2.94 ± 0.44	4.04 ± 0.82	(4.97 ± 0.58)					
18–20	(1.66 ± —)	(2.61 ± 0.38)	3.30 ± 0.60	(3.37 ± 0.13)	(7.64 ± 2.21)	(4.97 ± —)				
20–25	(1.90 ± 0.16)	(2.58 ± 0.39)	3.73 ± 0.80	(5.30 ± 1.37)	(7.20 ± 1.64)					
25–30		3.63 ± 0.76	5.26 ± 0.90							
30–35		(4.16 ± 0.34)	(5.01 ± —)	(7.34 ± —)						
35–40		(4.72 ± 0.13)	(5.47 ± 0.32)							
40–45		(5.93 ± 0.21)	(6.54 ± —)							
45–50			(8.25 ± 1.00)							

TABLE 3. Mean beam-filling corrections as a function of the initial data resolution and rainfall inhomogeneity for rain rates between 3 and 4 mm h^{-1}. The number of observations in each category is given in parentheses.

Data resolution	Rainfall inhomogeneity parameter					
	0.0–0.5	0.5–1.0	1.0–1.5	1.5–2.0	2.0–2.5	2.5–3.0
Plane parallel						
250 m	—	1.14 (2)	1.33 (8)	1.57 (1)	—	2.36 (1)
500 m	—	1.13 (2)	1.31 (8)	1.55 (1)	—	2.31 (1)
1 km	—	1.18 (4)	1.30 (6)	1.51 (1)	2.21 (1)	—
2 km	—	1.17 (4)	1.28 (7)	—	2.01 (1)	—
4 km	—	1.16 (7)	1.25 (4)	1.73 (1)	—	—
8 km	1.04 (1)	1.12 (9)	1.30 (2)	—	—	—
Slant path						
250 m	—	1.07 (2)	1.04 (8)	1.15 (1)	—	1.26 (1)
500 m	—	1.07 (2)	1.04 (8)	1.15 (1)	—	1.25 (1)
1 km	—	1.06 (4)	1.04 (6)	1.15 (1)	1.24 (1)	—
2 km	—	1.06 (4)	1.06 (7)	—	1.23 (1)	—
4 km	—	1.05 (7)	1.09 (4)	1.20 (1)	—	—
8 km	1.03 (1)	1.03 (9)	1.09 (2)	—	—	—

4.5-km freezing level, are no longer valid as these were coupled to the total liquid water content of a 4.5-km liquid column. Figure 4 shows the beam-filling correction for an inhomogeneity parameter of 1.0–1.5 with (panel a) the plane-parallel approximation and (panel b) the slant-path approximation as a function of the freezing level. As can be seen, the beam-filling correction decreases with decreasing freezing height for both approximations.

Because the conceptual cloud defined by Wilheit (1986) and used here has a constant rain rate in the column, the liquid water content scales nearly linearly with freezing height. The beam-filling correction for a 10 mm h^{-1} FOV with a 5-km freezing level should thus be very similar to a 20 mm h^{-1} FOV with a 2.5-km freezing level. Examination of Fig. 4 shows that both

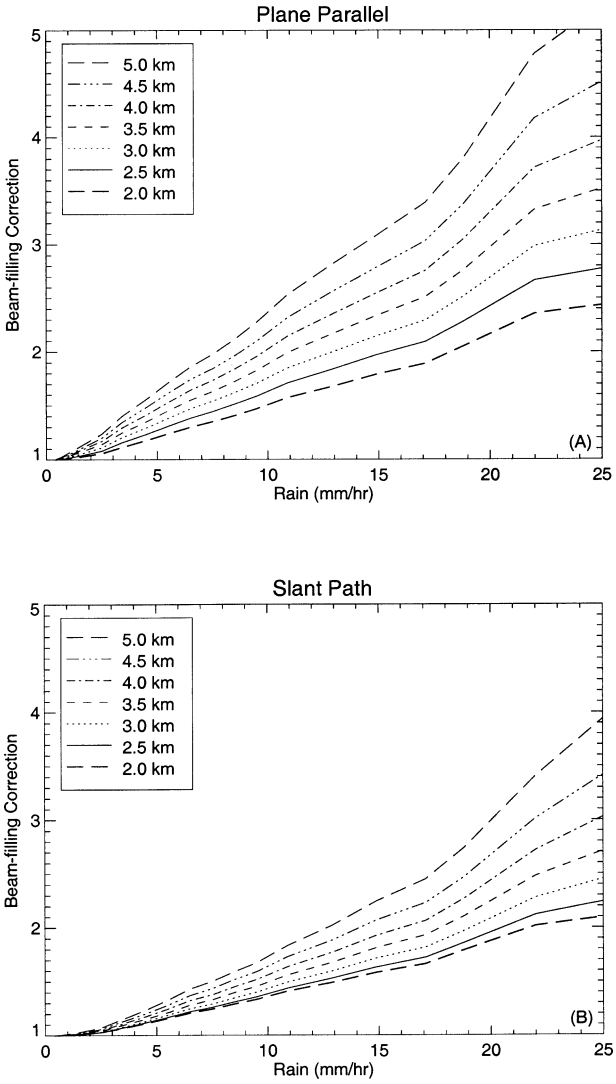

FIG. 4. Mean beam-filling corrections computed as a function of rainfall rate and freezing level. All curves are for an inhomogeneity parameter between 1.0 and 1.5: (a) plane-parallel and (b) slant-path computations.

TABLE 4. Mean beam-filling correction as a function of the initial data resolution and rainfall rate for plane-parallel and slant-path radiative transfer schemes. Results have been averaged over the observed inhomogeneity for each table entry.

Data resolution	Rainfall rate (mm h^{-1})			
	2–3	3–4	4–5	5–6
Plane parallel				
250 m	1.14	1.40	1.46	1.46
500 m	1.13	1.38	1.45	1.44
1 km	1.12	1.36	1.42	1.43
2 km	1.10	1.30	1.37	1.39
4 km	1.08	1.24	1.28	1.32
8 km	1.04	1.14	1.18	1.21
Slant path				
250 m	1.02	1.07	1.11	1.12
500 m	1.02	1.07	1.11	1.12
1 km	1.02	1.07	1.11	1.12
2 km	1.02	1.07	1.11	1.12
4 km	1.02	1.07	1.10	1.11
8 km	1.01	1.04	1.06	1.05

conditions yield a beam-filling correction of almost exactly 2.4. As such, the correction for lower freezing height can be simply inferred from any one height and the shape of the rain profile. Unfortunately, this is only approximately true for the slant-path approximation. As the freezing level decreases, so does the horizontal averaging that occurs when the slanted rays no longer cross neighboring pixels. This is easy to visualize for a 4-km PR pixel with a 500-m freezing level. Even at 50° incidence, only a small portion of the 4-km radiance will actually cross into neighboring pixels. As such, the slant-path and plane-parallel approximations converge in the limit that the freezing level is much smaller than the horizontal resolution of the data. This can be verified by comparing Figs. 4a and 4b for the lowest freezing level of 2.0 km.

Unfortunately, these results also imply that, for lower freezing levels, the slant-path calculations may also have some sensitivity to the initial resolution of the data as was shown in the previous section for plane-parallel calculations. While this issue cannot be addressed with the current data, the dependence should be relatively small since low freezing levels have generally small beam-filling corrections.

e. Sensitivity to cloud profiles

The previous section discussed the sensitivity of the beam-filling correction upon the liquid water column. The sensitivity to the ice loading can also be investigated. For this, the 4.5-km freezing level used in sections 2b–d is used again, but the ice amount is scaled to produce clouds with 25%, 50%, 200%, and 400% of the original clouds. Figure 5 shows the effect on the beam-filling correction for the same variability interval (1.0–1.5) as in the previous section. As can be seen from Fig. 5, the effect is quite small—especially considering that for a FOV of 24 km, 90% of the rain falls at rainfall rates less than 12 mm h^{-1}.

3. Global beam-filling corrections

Because the results of section 2 indicate that the mean beam-filling correction can be accurately predicted for the slant-path approximation using 4-km TRMM PR data, it is quite straightforward to use the results from Table 2 (plus equivalent tables for lower freezing levels) to compute beam-filling corrections that should be applied to 24-km TRMM radiometer FOVs on a pixel by pixel basis. Since beam-filling errors are not the only source of uncertainty, however, this study does not attempt any actual retrievals but instead uses the TRMM PR rainfall as the ''true'' rainfall and compares this to errors that would have resulted from the beam-filling uncertainty if high-resolution data were not available. The mean corrections applied when high-resolution data are not included are those derived in the earlier section from 3 months of oceanic TRMM PR data from December 1999 through February 2000. The freezing-level height dependence was incorporated in a straightforward manner by using the observed sea surface temperature (SST) and the same nominal lapse rate of 6.5 K km^{-1} used in the cloud profile.

In a pure radiometer algorithm, which was the only option before the launch of the TRMM satellite in 1997, or for radiometers other than the TMI, the subpixel inhomogeneity cannot be determined directly. In this case, it is necessary to apply a mean beam-filling correction based upon the inferred rainfall rate and freezing level only. This is defined as the ''RR + FL'' solution and is computed by using the average inhomogeneity parameter as a function of rain rate. This value is simply the average over the different inhomogeneities for each rain rate listed in Table 2 (and similar tables for different freezing levels) weighted by the probability of occurrence of each inhomogeneity in the training dataset. It represents the best value that a radiometer could retrieve on its own, without additional information regarding the actual variability within any given FOV. In addition to the RR + FL solution, there is an additional simplification that is possible if only the freezing level is used to compute a mean correction. This solution is the one implemented in the oceanic component of the microwave algorithm used in GPCP (Wilheit et al. 1991) as well as in TRMM 3A11 and AMSR-E. This simplification was necessary because the algorithm uses a histogram-based approach that does not explicitly retrieve a rainfall rate at each pixel. This solution is referred to as the ''FL only'' solution and is computed as the rainfall-weighted average over all rainfall rates and vari-

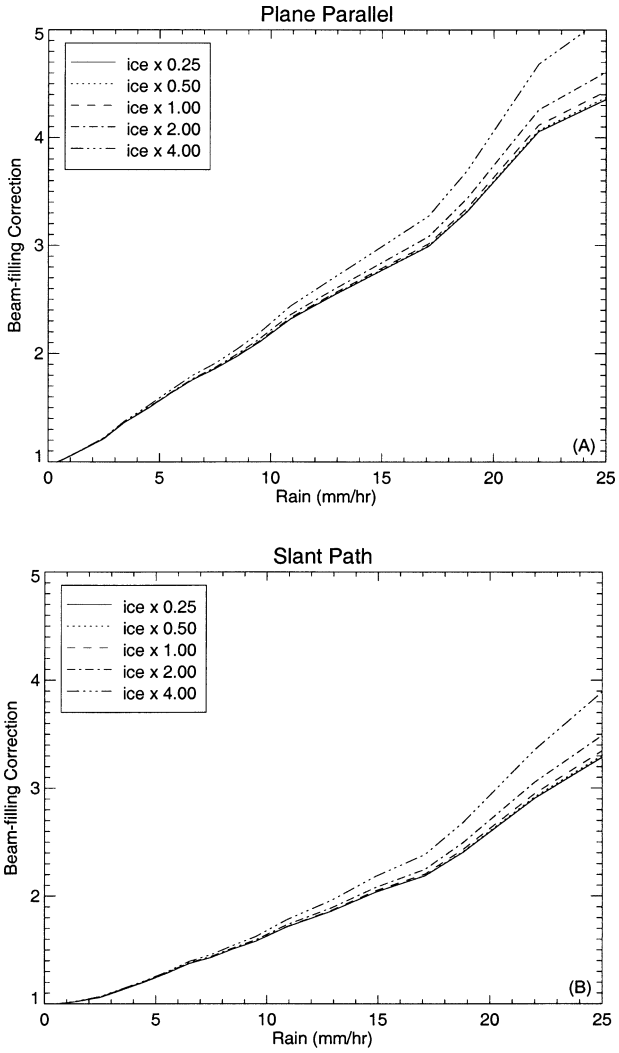

FIG. 5. Mean beam-filling corrections computed as a function of rainfall rate and a constant multiple of the original ice water content. All curves are for an inhomogeneity parameter between 1.0 and 1.5: (a) plane-parallel and (b) slant-path computations.

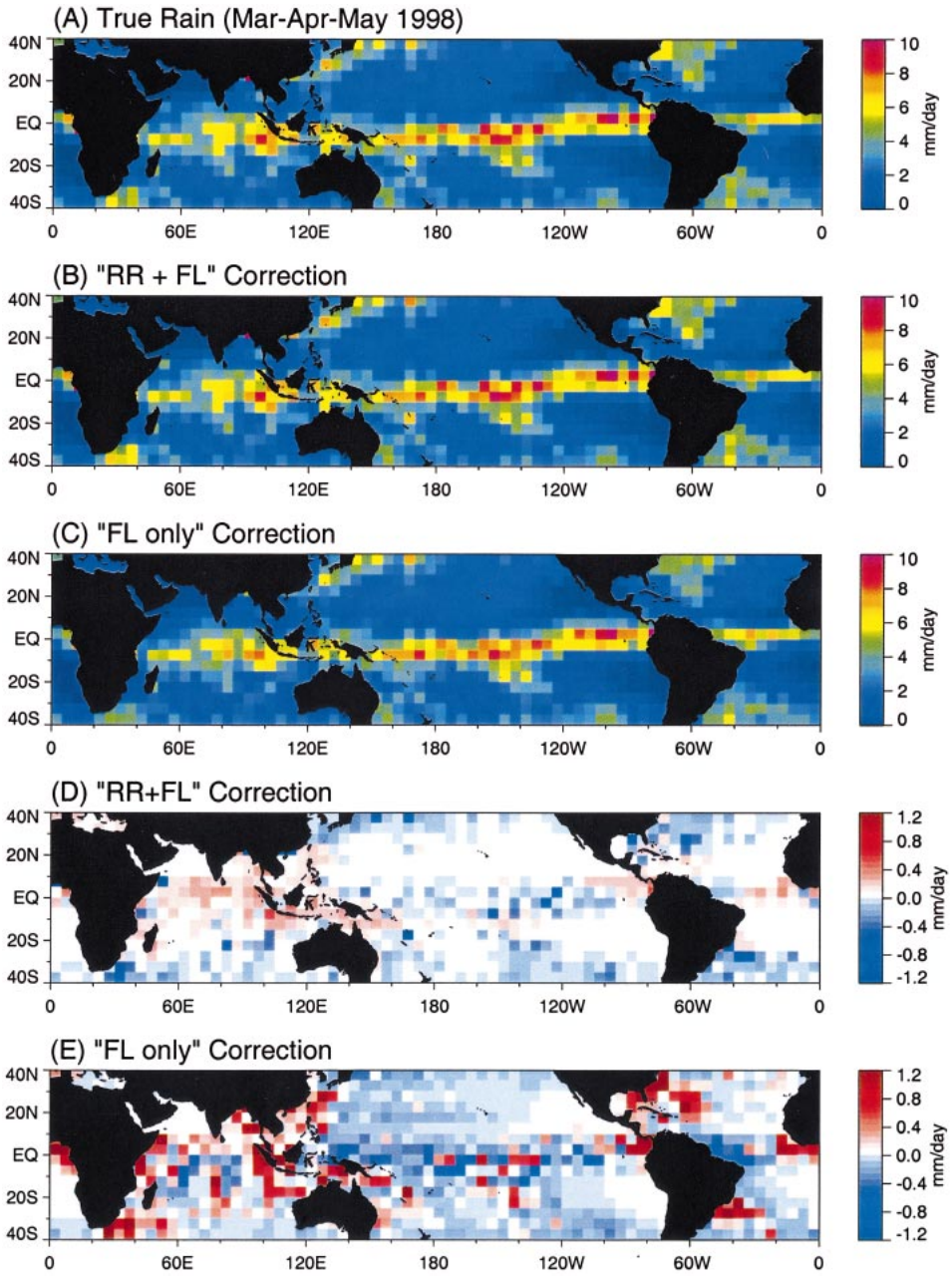

FIG. 6. Mean rainfall rates for MAM98 from (a) TRMM PR (assumed to be truth in this study), (b) a perfect radiometer algorithm that uses rainfall and freezing level to correct for sub-FOV rainfall inhomogeneity effects, and (c) a perfect radiometer algorithm that uses only the freezing level to correct for sub-FOV rainfall inhomogeneity effects. (d) Differences between (a) and (b); (e) differences between (a) and (c).

abilities listed in Table 2 (and equivalent tables for different freezing levels).

The above procedure computes the mean beam-filling correction for each pixel. The rainfall for each approximation is derived by dividing the true rainfall from the TRMM PR by the actual correction determined from the freezing level, rain rate, and rainfall variability, and then multiplying this value by either the RR + FL or the FL-only correction. Rain rates can then be accumulated over any space and time scale to examine potential errors at those scales. Here, the emphasis is on climate rainfall variability and seasonal averages over 3-month periods. Random effects are minimal at these large scales. Figures 6a–c show the true rainfall and the RR + FL solution, as well as the FL-only solution for the period of March–May of 1998 (MAM98). To first order, the three rainfall accumulation maps appear quite similar. This is not surprising since the pixel-level cor-

rections, while quite variable, have been averaged over a significant number of realizations to create monthly maps. The total rainfall accumulations of the three maps shown in Figs. 6a–c are remarkably constant. The total rain in the RR + FL solution is 1.5% lower than the true rainfall while the total rain in the FL-only solution is 0.9% higher. This is quite remarkable given that the beam-filling correction values were computed from only the center pixel positions of the TRMM PR during the December 1999–February 2000 period. Such a constant result appears to indicate that both the rainfall variability, which is responsible for variation in the RR + FL map, as well as the conditional rainfall rate, which is responsible for most of the differences in the FL-only map, remain relatively constant on a global scale.

Despite the small differences at the global scale, larger regional differences are noticeable. Figures 6d and 6e display the differences between the true rain and the RR + FL solution as well as the FL-only solution, respectively. As can be seen, significant differences exist over large regions. Red areas in Fig. 6d indicate areas where the RR + FL solution is lower than the true rain. Given the general trend of increasing beam-filling corrections with increasing variability, red areas in Fig. 6d are thus areas where the actual rainfall variability for observed rainfall rates is greater than the mean value [derived during December–February (DJF) 1999/2000]. Generally speaking, most of these areas appear concentrated in the Indian Ocean, the Maritime Continent, and the ITCZ areas just west of South America and Africa.

In contrast to the difference maps of the RR + FL solution, the FL-only solution shows a very distinct pattern. This pattern reflects, to first order, the regional differences in conditional mean rain rates. Results from Table 4, as well as earlier work by Chiu et al. (1990), clearly show the dependence of the beam-filling correction upon rainfall rate. Since large accumulations can be the result of either continuous light rain or occasional heavy rain, these biases are also present in the rainfall accumulations that do not consider these differences.

In keeping with the original goals of this paper, Fig. 7a examines the tropical oceanic mean rainfall variability that is artificially introduced into rainfall climatologies by an incomplete knowledge of the subpixel variability for the two solutions discussed previously. As was the case with the MAM98 period discussed previously, there is very little variability on the global monthly scale examined in this figure. The magnitude of the error introduced by the unknown rainfall inhomogeneity within a given radiometer FOV for the RR + FL solution (solid curve) is seen to be exceedingly small, rarely exceeding 0.5% on a monthly global scale. This implies that on a global monthly basis, variations in the rainfall inhomogeneity do not change sufficiently to cause differences between radar and radiometer rainfall products such as those examined in Fig. 1. The dashed line in Fig. 7a shows the corresponding results for the FL-only solution. Its variability is slightly larger,

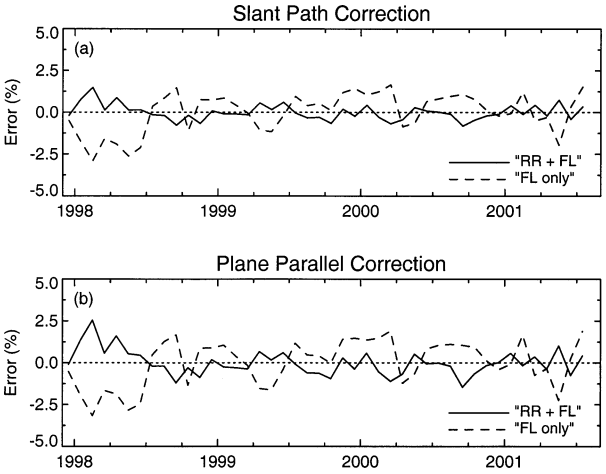

FIG. 7. Monthly errors introduced into the global mean oceanic rainfall (40°N–40°S) by incomplete knowledge of the sub-FOV inhomogeneity. Solid lines are for the correction that uses rain rates and freezing level while dashed lines are for the correction that uses only the freezing level. (a) Slant-path radiative calculations and (b) plane-parallel calculations.

amounting to slightly less than 2% during the El Niño period in early 1998. This again is driven primarily by a slightly higher mean conditional rainfall rate during this period.

Figure 7b shows the same results but using the plane-parallel approximation to compute the beam-filling correction as described in section 2. The results are nearly identical to those shown in Fig. 7a, except that the plane-parallel assumption leads to slight increases in the magnitude of the monthly variations. Still, even for the El Niño period in early 1998, the global biases introduced by the FL-only correction (dashed line) and plane-parallel assumption amount to no more than approximately 2%.

Regionally, however, biases introduced by the unknown rainfall inhomogeneity can be significantly larger. If one concentrates on the Indian Ocean, for instance, one can see a significantly different picture. Figures 8a and 8b show the same results as those in Fig. 7, but for an area between 0° and 20°N and 70° and 110°E intended to represent the Indian Ocean. Unlike the global mean values, this region is seen to vary far more significantly and systematically over the 4-yr time period. The slant RR + FL solution is seen to underestimate the true rainfall by about 2.5% on average, but with monthly variations of up to 10%. More dramatic is the bias introduced by the plane-parallel, FL-only solution. Here, the mean bias over the Indian Ocean is approximately 10% but with a monthly deviation of another 10%–15%. From a practical point of view, it is thus possible to make significant regional errors, particularly if less desirable corrections such as the plane-parallel FL-only solution are implemented.

In order to get a more complete picture of regions that might be susceptible to climate-scale biases, Fig. 9

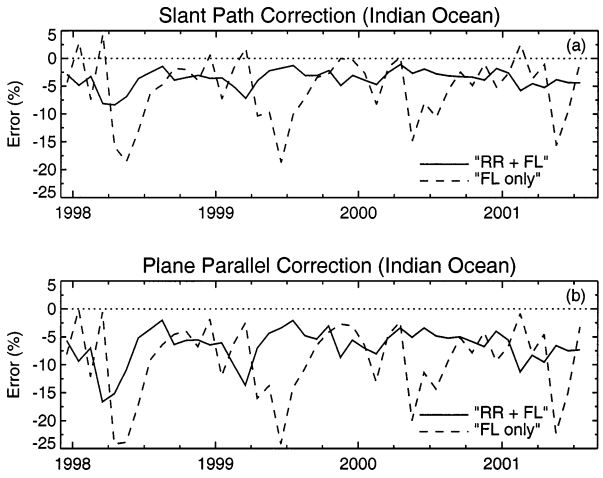

FIG. 8. Monthly errors for the Indian Ocean (0°–20°N, 130°–170°E) by incomplete knowledge of the sub-FOV inhomogeneity. Solid lines are for the correction that uses rain rates and freezing level while dashed lines are for the correction that uses only the freezing level. (a) Slant-path radiative calculations and (b) plane-parallel calculations.

shows difference maps similar to those shown in Fig. 6 for MAM98, but averaged over the entire 44-month time period from December 1997 through July 2001 examined in this study. This time period represents TRMM data while the satellite was at an altitude of 350 km. Data after July 2001 are from a 400-km altitude and were not used because they have slightly lower spatial resolution that could impact the conclusions. Results from the 44 months are quite similar to those found in the MAM98 period. For the RR + FL solution, there is a low bias in the Indian Ocean, the Maritime Continent, the Caribbean, and the western extensions of the ITCZ from South America and Africa. This may be a result of the somewhat more continental nature of the convection as it moves from the continents into the sea. This is illustrated even more dramatically with the FL-only correction where all the areas of underestimation (red) are in close proximity to the continents where higher conditional rainfall rates are known to exist.

4. Summary and discussions

Rainfall validation has historically involved comparison of satellite estimates with a set of observations made from the ground in order to gain confidence as well as to assign error statistics to satellite products.

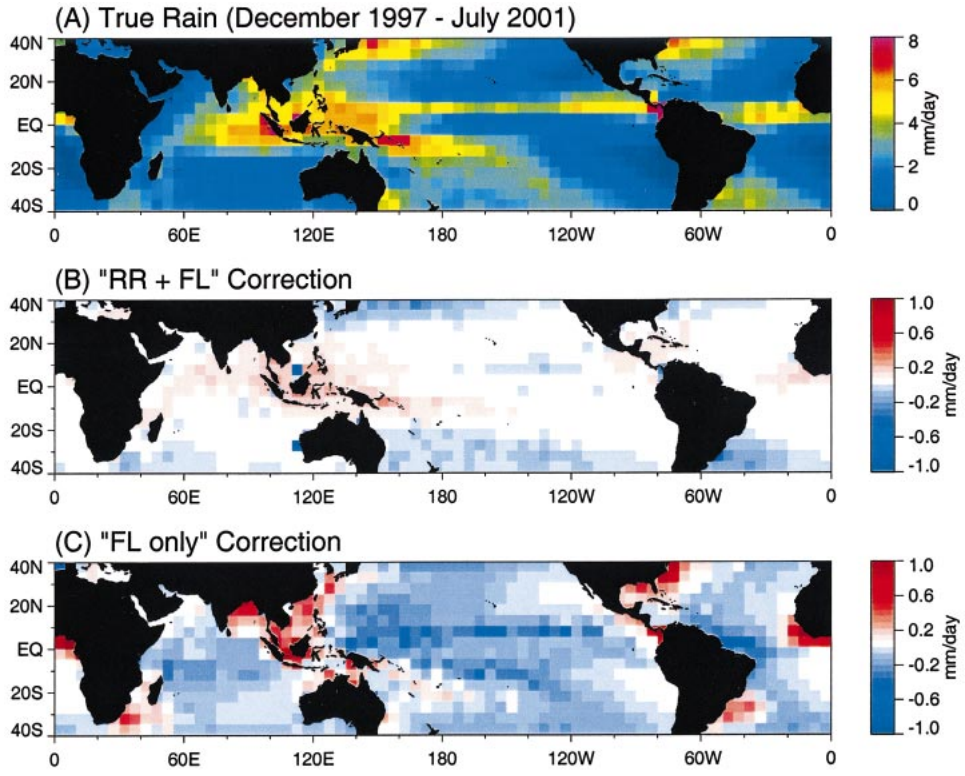

FIG. 9. (a) Mean rainfall rates for Dec 1998–Jun 2002 from TRMM PR (assumed to be truth in this study). (b) The differences between the ''true'' rainfall and a perfect radiometer algorithm that uses rainfall and freezing level to correct for sub-FOV rainfall inhomogeneity effects. (c) Same as in (b) but for a radiometer algorithm that uses only the freezing level to correct for sub-FOV rainfall inhomogeneity effects.

This paradigm has problems. First, it has proven to be extremely difficult to make accurate ground-based measurements of precipitation. Sparse gauges often correlate poorly with satellite observations due to large discrepancies between the space and time scales of the two instruments. More important, however, may be the fact that algorithm errors are not constant in space and time, but have a regional and time-dependent character. Validation sites, unless they account for this variability, will observe only one point of what is in reality a complex tapestry of biases that are introduced by observations that are not fully constrained and are thus susceptible to errors due to changing cloud characteristics. Without complete knowledge of what these changing cloud characteristics may be and how they affect rainfall retrieval schemes, it is therefore very difficult to have confidence in the representativeness of a small number of ground-based comparisons.

The above issues have led to a physical validation approach, which attempts to explicitly model the uncertainty in satellite rain products by examining each assumption separately and then using error propagation methods to derive the final uncertainty. Within this framework, the aliasing of derived rainfall due to sub-FOV rainfall inhomogeneity has been identified as a key parameter that was theoretically well understood but for which the uncertainty at various time and space scales had not been quantified. To that end, the current study reviewed the theoretical basis for the correction and then examined TRMM PR data as the source of sub-FOV rainfall data to assess the impact of this rainfall inhomogeneity upon climate-scale rainfall errors.

Using PR data, the beam-filling correction was found to closely match previous studies that used a plane-parallel approach for computing T_b based upon 4-km ground-based radar data. The differences between an earlier study by Chiu et al. (1990) showed greater variations between two periods of the GATE experiment than with the current study using 3 months of global 4-km TRMM PR data. When plane-parallel calculations were replaced by more correct slant-path calculations, however, the beam-filling bias was reduced from a factor of approximately 1.52 to a value of 1.26. This effectively reduces the total uncertainty attributable to the beam-filling uncertainty.

From an error modeling perspective, it was shown that individual pixels could have very large variations due to the unknown rainfall inhomogeneity. Based upon Table 2, for instance, a T_b consistent with 5 mm h^{-1} in the case of homogeneous rainfall is also consistent with $5 \times 3.56 = 17.8$ mm h^{-1} if the inhomogeneity parameter is in the 2.5–3.0 range. A single pixel thus has an uncertainty of this magnitude but such calculations say little about how these errors should be propagated to larger time and space scales unless direct measurements or proxy variables can be found to examine this question.

Because results from section 2 indicated that 4-km data have sufficient resolution (when slant-path calculations are used) to fully describe the beam-filling correction, the TRMM PR was used to analyze variations at long time and space scales. The 44-month average bias was shown in Fig. 9. The figure clearly shows that areas of systematically larger than average inhomogeneity exist in those regions that are thought to have some continental traits. This is particularly apparent in the correction that uses only the freezing level. This correction is susceptible to changes in both the mean conditional rain as well as to changes in the rainfall inhomogeneity within a given rain-rate category.

Perhaps a bit surprising, however, was the fact that globally the beam-filling correction does not appear to vary by more than a few percent irrespective of the analysis method. Thus, while regional variations, as analyzed over a $20^\circ \times 40^\circ$ area encompassing the Indian Ocean, can be quite dramatic and aliased relative to the global mean, globally these changes appear to cancel to produce a very robust signal. The question raised in the introduction regarding the possibility that beam-filling biases might be responsible for the observed differences between TRMM radar and radiometer products can now be answered. Beam-filling biases cannot be responsible for this discrepancy as Fig. 7 clearly shows that actual changes in rainfall variability cannot account for more than a 2.5% change in global oceanic rainfall, while the ENSO discrepancy is on the order of 10%.

Despite the success of the current study in defining uncertainties due to rainfall variability at different space and time scales, the problem is of course, not solved. The rainfall inhomogeneity is but one of the sources of uncertainty that must be considered. Other sources of uncertainty, such as the shape of the rainwater profile, the amount of cloud water, the excess absorption caused by melting particles, and the density and drop spectra of ice particles, to name the most important sources of uncertainty, all need to be analyzed in a similar fashion. Some of these will not have readily accessible sources of data. In these cases, a proxy variable will have to be determined from ground observations first before a global analysis and a corresponding global error model can be constructed. Nonetheless, these regional biases need to be understood. Without them, regional biases determined from ground-based sensors (such as perhaps a low bias in the Indian Ocean) cannot be put into the proper global framework needed to fully assess global satellite-derived rainfall products.

Acknowledgments. This work was supported by the TRMM program under NASA TRMM Grants NAG5-11189 and NAG-13694.

REFERENCES

Bauer, P., L. Schanz, and L. Roberti, 1998: Correction of three-dimensional effects for passive microwave remote sensing of convective clouds. *J. Appl. Meteor.*, **37,** 1619–1632.

Chang, A. T. C., and L. S. Chiu, 2001: Non-systematic errors of monthly oceanic rainfall derived from passive microwave radiometry. *Geophys. Res. Lett.*, **28,** 1223–1226.

Chen, R., 2003: Beamfilling correction study for retrieval of oceanic rain from passive microwave observations. Ph.D. dissertation, Texas A&M University, 49 pp.

Chui, L. S., G. R. North, D. A. Short, and A. McConnell, 1990: Rain estimation from satellites: Effects of finite field of view. *J. Geophys. Res.*, **95,** 2177–2185.

Graves, C. E., 1993: A model for the beam-filling effect associated with the microwave retrieval of rain. *J. Atmos. Oceanic Technol.*, **10,** 5–14.

Ha, E., and G. R. North, 1995: Model studies of the beam-filling error for rain-rate retrieval with microwave radiometers. *J. Atmos. Oceanic Technol.*, **12,** 268–281.

Huffman, G. J., and Coauthors, 1997: The Global Precipitation Climatology Project (GPCP) combined precipitation dataset. *Bull. Amer. Meteor. Soc.*, **78,** 5–20.

Kummerow, C., 1993: On the accuracy of the Eddington approximation for radiative transfer in the microwave frequencies. *J. Geophys. Res.*, **98,** 2757–2765.

——, 1998: Beamfilling errors in passive microwave rainfall retrievals. *J. Appl. Meteor.*, **37,** 356–370.

——, and Coauthors, 2000: The status of the Tropical Rainfall Measuring Mission (TRMM) after two years in orbit. *J. Appl. Meteor.*, **39,** 1965–1982.

——, and Coauthors, 2001: The evolution of the Goddard Profiling Algorithm (GPROF) for rainfall estimation from passive microwave sensors. *J. Appl. Meteor.*, **40,** 1801–1820.

Liebe, H. J., G. A. Hufford, and M. G. Cotton, 1993: Propagation modeling of moist air and suspended water/ice particles at frequencies below 1000 GHz. *AGARD Conf. Proc.*, **542,** 3.1–3.10.

Marshall, J. S., and W. M. Palmer, 1948: The distribution of raindrops with size. *J. Meteor.*, **5,** 165–166.

Matrosov, S. Y., K. A. Clark, B. E. Martner, and A. Tokay, 2002: X-band polarimetric radar measurements of rainfall. *J. Appl. Meteor.*, **41,** 941–952.

Mie, G., 1908: Beiträge zue Optik Trüber Medien, speziell kolloidaler Metalösungen. *Ann. Phys.*, **26,** 597–614.

North, G. R., and I. Polyak, 1996: Spatial correlation of beam-filling error in microwave rain-rate retrievals. *J. Atmos. Oceanic Technol.*, **13,** 1101–1106.

Petty, G. W., 1994: Physical retrievals of over-ocean rain rate from multichannel microwave imagery. Part I: Theoretical characteristics of normalized polarization and scattering indices. *Meteor. Atmos. Phys.*, **54,** 79–99.

Roberti, L., J. Haferman, and C. Kummerow, 1994: Microwave radiative transfer through horizontally inhomogeneous precipitating clouds. *J. Geophys. Res.*, **99,** 16 707–16 718.

Robertson, F. R., D. E. Fitzjarrald, and C. D. Kummerow, 2003: Effects of uncertainty in TRMM precipitation radar path integrated attenuation on interannual variation of tropical oceanic rainfall. *Geophys. Res. Lett.*, **30,** 1180, doi:10.1029/2002GL016416.

Smith, E. A., P. Bauer, F. S. Marzano, C. D. Kummerow, D. McKague, A. Mugnai, and G. Panegrossi, 2002: Intercomparison of microwave radiative transfer models for precipitating clouds, *IEEE: Trans. Geosci. Remote Sens.*, **40,** 541–549.

Soden, B. J., 2000: The sensitivity of the tropical hydrologic cycle to ENSO. *J. Climate*, **13,** 538–549.

Spencer, R. W., B. B. Hinton, and W. S. Olson, 1983: Nimbus-7 37 GHz radiances correlated with radar rain rates over the Gulf of Mexico. *J. Climate Appl. Meteor.*, **22,** 2095–2099.

Wang, S. A., 1996: Modeling the beam filling correction for microwave retrieval of oceanic rainfall. Ph.D. dissertation, Texas A&M University, 100 pp.

Wilheit, T. T., 1986: Some comments on passive microwave measurement of rain. *Bull. Amer. Meteor. Soc.*, **67,** 1226–1232.

——, A. T. C. Chang, and L. S. Chiu, 1991: Retrieval of monthly rainfall indices from microwave radiometric measurement using probability distribution functions. *J. Atmos. Oceanic Technol.*, **8,** 118–136.